Journal of Materials Chemistry A

Accepted Manuscript

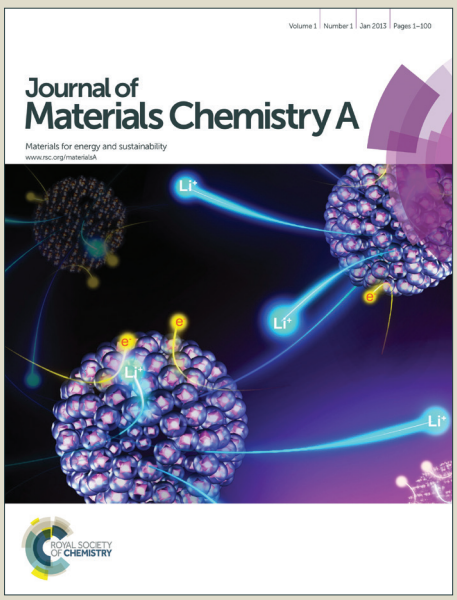

ROYAL SOCIETY OF CHEMISTRY

www.rsc.org/materialsA

Journal Name

ARTICLE

Visible-light-driven BiOBr nanosheets for highly facet-dependent photocatalytic inactivation of *Escherichia coli*

Received 00th January 20xx,
Accepted 00th January 20xx

DOI: 10.1039/x0xx00000x

www.rsc.org/

Dan Wu,[a] Bo Wang,[a] Wei Wang,[*ab]Taicheng An,[*c]Guiying Li,[c]TszWai Ng,[a]Ho Yin Yip,[a] Chunmei Xiong,[b] Hung Kay Lee[d] and Po Keung Wong*[a]

Bismuth oxybromide (BiOBr) nanosheets with fully exposed {001} and {010} facets are synthesized via a facile hydrothermal method. Significant differences in photocatalytic inactivation towards *Escherichia coli* K-12 under visible light irradiation are found to be highly dependent on the dominantly exposed facets. In comparison with BiOBr with dominant {010}-facet (B010) nanosheets, BiOBr with dominant {001}-facet(B001) nanosheets exhibit remarkably higher photocatalytic activity in bacterial inactivation. The superior activity is ascribed to the more favorable separation and transfer of photogenerated electron-hole pairs as well as more oxygen vacancies of B001 nanosheets. Due to the faster production and further accumulation of $\bullet O_2^-$ and h^+ within a short time, VLD photocatalystof B001 nanosheets can completely inactivate 10^7 colony forming unit (CFU) mL^{-1} (i.e. 7-log reduction) bacterial cells within 2 h; while only 1- and 6.5-log reduction of bacterial cells can be achieved within 2 and 6 h, respectively, by B010 nanosheets due to limited amount of h^+ and $\bullet O_2^-$ generated.

Introduction

Semiconductor photocatalysts have received considerable attention due to their wide applications in solar energy conversion and environmental remediation.[1,2] As photocatalytic reactions taking place on the surfaces of semiconductors, the surface atomic structure of photocatalysts plays a critical role in determining the photocatalytic activity. This is because surface atom coordination and arrangement intrinsically determine the adsorption of reactant molecules and desorption of product molecules, and the surface transfer between the reactant molecules and photoexcited electrons.[3-5] Hence, the photocatalytic activities of semiconductor photocatalyst crystals are highly sensitive to the expression of specific crystal facets, which exhibit different atomic configurations and surface structures. Recently, great interest has attracted to simply control crystal facets of photocatalysts to explore their full potentials in the photocatalytic applications.[3-8] For example, the single-crystalline Ag_3PO_4 rhombic dodecahedrons with only {110} facets exposed exhibited much higher photocatalytic activities than the Ag_3PO_4 cubes bounded entirely by {100} facets for the degradation of Methyl Orange (MO) and Rhodamine B (RhB).[6] Anatase TiO_2 with co-exposed {101} and {001} facets had enhanced photocatalytic CO_2 reduction activity.[7] Reduction and oxidation co-catalysts selectively deposited on the {110} and {010} facets of $BiVO_4$ resulted in much higher photocatalytic activity in water oxidation reactions.[8] Besides, the facet-dependent photocatalytic activity of a large number of photocatalysts, such as ZnO,[9] $SrTiO_3$,[10] WO_3,[11]InOCl,[12] Ag_2O,[13] BiOCl,[14] Cu_2O,[15] InOOH,[16] AgBr[17] and specially TiO_2,[18,19] have been reported. As a result, crystal facet engineering of semiconductors fully exposed with reactive facets opens up promising possibilities for developing new photocatalysts with highly improved activity. However, the percentage of highly reactive facets in the final photocatalyst has still been relatively low at present. It is interestingly to mention that sheet-like crystals and extremely high two-dimensional anisotropy can provide reactive sites approaching 100% on the surface of photocatalysts.[20] The large-area non-stoichiometry on the surface will result in intriguing properties. Nevertheless, unmet challenges still remain both in the fabrication of photocatalyst nanosheets with a high exposure of specific crystal facets and the exploration of underlying mechanisms of facet-dependent photocatalytic performance.

Recently, bismuth oxybromide (BiOBr) has attracted a remarkable interest due to its excellent photocatalytic activity and chemical stability under visible light (VL) irradiation.[20-24]

[a] School of Life Sciences, The Chinese University of Hong Kong, Shatin, NT, Hong Kong SAR, China.E-mail: pkwong@cuhk.edu.hk;
[b] College of Materials Science and Engineering, Huazhong University of Science and Technology, Wuhan 430074, China. E-mail: weiwang@hust.edu.cn;
[c] State Key Laboratory of Organic Geochemistry and Guangdong Key Laboratory of Environmental Resources Utilization and Protection, Guangzhou Institute of Geochemistry, Chinese Academy of Sciences, Guangzhou 510640, China. E-mail: antc99@gig.ac.cn;
[d] Department of Chemistry, The Chinese University of Hong Kong, Shatin, NT, Hong Kong SAR, China. E-mail: hklee@cuhk.edu.hk

∗Electronic Supplementary Information (ESI) available. See
DOI: 10.1039/x0xx00000x

The unique visible-light-driven (VLD) photocatalytic performance of BiOBr is highly structure-dependent, attributing to its layered structure interleaved with $[Bi_2O_2]$ slabs and double Br atoms slabs along the *c*-axis.[21-25] Recent studies revealed that different facets of BiOBr crystals exhibited distinct photocatalytic activities.[26-28] For instance, BiOBr with dominantly exposed {102} facets were superior in the photocatalytic activity for the degradation of RhB than that of BiOBr with {001} facets.[26] Comparing with BiOBr exposed with {010} facet, BiOBr with {001} dominant exposed-facets exhibited much higher photocatalytic activity in degrading 2,4-dichlorophenol under UV light.[27]However, all the present reports concerning BiOBr photocatalysts with different exposed facets just focused on the photoactivity tests to degrade various organic pollutants, for example, 2,4-dichlorophenol,[27] synthetic dyes such as MO,[28,29] RhB[26,29-32] and Methyl Blue.[29,30] To the best of our knowledge, the facet effect on VLD photocatalytic bacterial inactivation properties of BiOBr has never been attempted yet.

In this study, BiOBr nanosheets with high percentage exposed {001} and {010} facets were synthesized via a simple hydrothermal method. The facet-dependent VLD photocatalytic inactivation activities of these BiOBr nanosheets were assessed using a model bacterium, *Escherichia coli* K-12. The dominant reactive species involved in the facet-dependent photocatalytic bacterial inactivation were also identified. Accordingly, a reasonable mechanism was proposed to well explain the significant differences in VLD photocatalytic bacterial inactivation performance between {001}- and {010}-facet exposed BiOBr nanosheets.

Experimental

Synthesis of BiOBr nanosheets

BiOBr nanosheets were prepared via a hydrothermal method. In a typical procedure, 1.94 g $Bi(NO_3)_3{\cdot}5H_2O$ was dissolved in 10 mL HNO_3 aqueous solution (1 M) with stirring. Then 50 mL KBr aqueous solution (0.01 M) was added into the above solution followed by stirring for 0.5 h at room temperature (*ca.* 25 °C). After that, the solution was transferred into a 100 mL Teflon-sealed autoclave and heated at 160 °C for 12 h. After cooling to the room temperature, the precipitate was centrifuged, washed with distilled water and then with anhydrous ethanol for several times, before dried at 60 °C in an oven. The obtained product was denoted as B001. The synthesis of B010 sample used the similar procedure except that NaOH aqueous solution (2 M) was added to the mixture to adjust pH value to 6 before being transferred to the Teflon-sealed autoclave. All the chemicals used in the experiments were of reagent grade and used as received without further purification.

Characterizations of BiOBr nanosheets

The X-ray diffraction (XRD) patterns of as-prepared samples were determined by a SmartLab X-ray diffractometer (Rigaku, Tokyo, Japan) operating at 40 mA and 40 kV with Cu Kα as radiation source. Morphologies of the prepared samples were observed using Quanta 400F field-emission scanning electron microscopy (SEM) (FEI, Hillsboro, OR, USA), Tecnai G2 Spirit transmission electron microscopy (TEM) (FEI, Hillsboro, OR, USA), and Tecnai F20 high resolution TEM (HRTEM) (FEI, Hillsboro, OR, USA). UV-vis diffuse reflectance spectra (DRS) of the samples were measured with a Varian Cary 500 UV-vis spectrophotometer (Palo Alto, CA, USA) equipped with a Labsphere diffuse reflectance accessory. The Brunauer-Emmett-Teller (BET) specific surface area of the samples were determined by an ASAP 2020 volumetric adsorption analyzer (Micromeritics, Norcross, GA, USA). The Raman spectra of the samples were measured using a LabRAM HR800 Raman spectrometer (Horiba JobinYvon, Villeneuve d'Ascq, France) with the excitation of a 532 nm laser beam. X-ray photoelectron spectroscopy (XPS) analysis was acquired on an AXIS-ULTRA DLD-600W spectrometer (Shimadzu–Kratos, Japan). Electron paramagnetic resonance (EPR) spectra were recorded on a Bruker EMX EPR spectrometer equipped with a variable temperature helium flow cryostat system (Oxford Instruments). The transient photocurrent responses and electrochemical impedance spectroscopy (EIS) measurements of the samples were determined using a CHI760C electrochemical working station (CH Instruments, Shanghai, China) in a three-electrode quartz cells with Na_2SO_4 (0.1 M) electrolyte solution. The working electrode was BiOBr nanosheets deposited on a fluorinated-tin-oxide (FTO) conducting glass. Ag/AgCl and Pt were used as the reference and the counter electrodes, respectively, for the measurements.

Photocatalytic inactivation activity of BiOBr nanosheets

The visible-light-driven photocatalytic inactivation of *E. coli* K-12 by BiOBr nanosheets was conducted under fluorescent tubes (15 W, FSL, Foshan, China) irradiation. The VL intensity was measured by a LI-250 light meter (LI-COR, Lincoln, Nebraska, USA) and was adjusted at an intensity of 8.1 mW cm^{-2} for the experiments. The bacterial strain of *E. coli* K-12 was inoculated into 50 mL of Nutrient Broth (Lab M, Lancashire, UK) and incubated at 37 °C for 15 h in a shaking incubator. The bacterial cells were harvested by centrifugation for 1 min in an Eppendorf tube by a Z323 microcentrifuge (HermleLabortechnik GmbH, Wehingen, Germany), and then washed twice with sterilized saline (0.9% NaCl) solution. Finally the cell pellet was re-suspended in sterilized saline solution. The final cell density was adjusted to about 1×10^7 colony forming unit (CFU) mL^{-1}. A suspension (50 mL) containing the bacterial cells and the photocatalyst (50 mg) in a flask was placed in dark under continuous stirring for 0.5 h to reach the adsorption equilibrium. Then the VL was turned on to start the photocatalytic inactivation experiments. At different time intervals, aliquots of the sample were collected and serially diluted with sterilized saline solution. The sample was serially diluted with sterilized saline solution and 0.1 mL of the diluted samples was immediately spread on Nutrient Agar (Lab M, Lancashire, UK) plates and then incubated at 37 °C for 24 h to determine the number of survival cells. For comparison, light

controls (bacterial cells and light without photocatalyst) and dark controls (photocatalyst and bacterial cells without light) were also included in the study. To identify the dominant reactive species accounting for the photocatalytic bacterial inactivation, specific compounds (i.e. respective reactive species scavengers) at optimized concentration was added individually under otherwise identical conditions mentioned above. All the above experiments were conducted in triplicates.

Analysis method and recognizing reactive oxygen species (ROSs)

H_2O_2 produced during the photocatalytic inactivation process was analyzed by a highly sensitive fluorometric method.[33] Briefly, 0.4 mL of the samples, 0.1 mL of coumarin (0.5 mM), and 0.1 mL of $FeSO_4$ (0.25 mM) were added into 0.4 mL of citrate buffer (pH 3) with further standing at room temperature for 10 min. Then the mixture was measured at emission wavelength of 456 nm with excitation wavelength of 346 nm by an Infinite® M200 microplate reader (Tecan, Männedorf, Switzerland). The concentration of produced H_2O_2 was calculated based on the standard as the same procedure using pure H_2O_2 as a reference.

To detect the production of hydroxyl radical (•OH), 50 mg of BiOBr nanosheet sample was suspended in a 50 mL saline containing terephthalic acid (TA) (0.5 mM) and NaOH (2 mM).[22] The resulting suspension was then exposed to VL irradiation. At regular intervals, 1 mL of the suspension was collected and centrifuged to separate the photocatalyst. Finally, the fluorescence of the solution was measured spectrophotometrically at emission wavelength of 456 nm with excitation wavelength of 315 nm by an Infinite® M200 microplate reader.

To detect the production of superoxide radical ($\bullet O_2^-$), the procedure was similar to that of •OH, except nitroblue tetrazolium (NBT) was used instead of TA and NaOH.[22] The production of $\bullet O_2^-$ was quantitatively analyzed by detecting the decrease of the concentration of NBT at wavelength of 259 nm with a Bluestar A UV–Vis spectrophotometer (LabTech, Tianjin, China).

Results and discussion

Characterizations of BiOBr nanosheets

Fig. 1 shows the XRD patterns of as-prepared B001 and B010 samples. All the peaks can be well indexed to the tetragonal phase of BiOBr (PDF 00-009-0393). The intense and sharp diffraction peaks imply that the as-prepared B001 and B010 samples are well-crystallized. Moreover, no peaks from the impurities are observed, indicating high purity of the as-prepared samples.

SEM images reveal that B001samples are sheet-shaped structures with the width of 1.5-3.5 μm and thickness of 100-200 nm, while B010 samples are also nanosheets with the width of 0.8-1.5 μm and thickness of 20-50 nm (Fig. S1). TEM image of an individual B001 nanosheet further confirms its sheet-shaped structure (Fig. 2a). The clear lattice fringes with an inter-planar lattice spacing of 0.278 nm and the angle of 90°corresponds to the (110) atomic planes (Fig. 2b). The corresponding selected-area electron diffraction (SAED) pattern in Fig. 2c reveals single-crystalline characteristic of B001 nanosheet. The angle labeled in SAED pattern is estimated to be 45°, which is in good agreement with the theoretical value of the angle between the {110} and {200} planes. The set of diffraction spots can be indexed as the [001] zone axis. Based on the above results and the symmetries of tetragonal BiOBr, we can deduce that the top and bottom surfaces of B001 nanosheets are {001} facets, while the four lateral surfaces are {110} facets. The B010 nanosheets are also confirmed by TEM image (Fig. 2d) and demonstrated to be single crystals with high crystallinity (Fig. 2e). The inter-planar lattice spacing of 0.282 nm can be assigned to the {102} planes of the B010nanosheet. Since the interfacial angle of 45.9° between {102} and {002} planes matches well with the theoretical value, the corresponding SAED pattern (Fig. 2f) can be indexed as the [010] zone axis. Hence, the dominant facets of B001and B010 nanosheets can be identified as {001} and {010} planes, respectively. The area percentage of the dominant {001} facets is geometrically calculated to be 97% for the B001 nanosheets, while the dominant {010} facets are 98% for the B010 nanosheets.

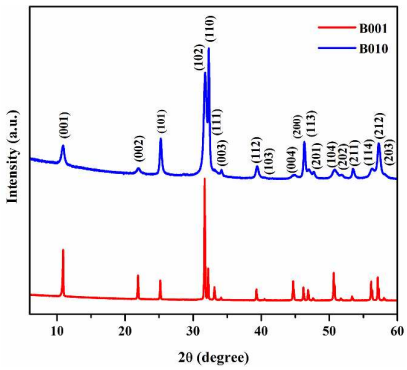

Fig. 1 XRD patterns of B001 and B010 nanosheets.

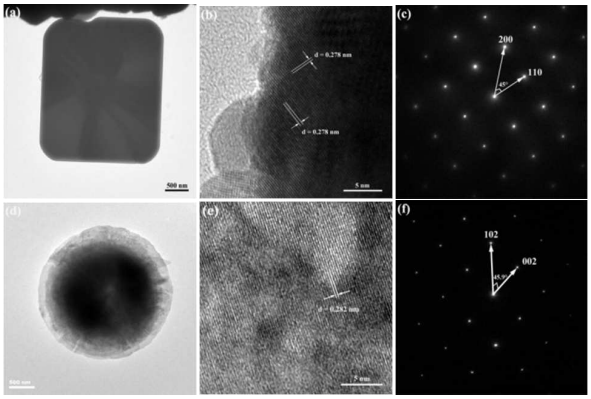

Fig. 2 (a) TEM image, (b) HRTEM image and (c) corresponding SAED pattern of B001 nanosheet, (d) TEM image, (e) HRTEM image and (f) corresponding SAED pattern of B010 nanosheet.

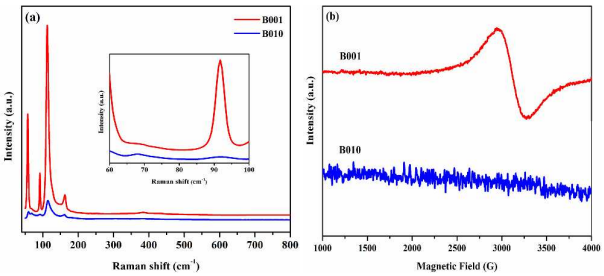

Fig. 3 (a) Raman spectra and (b) Powder EPR spectra (at 77° K) of B001 and B010 nanosheets.

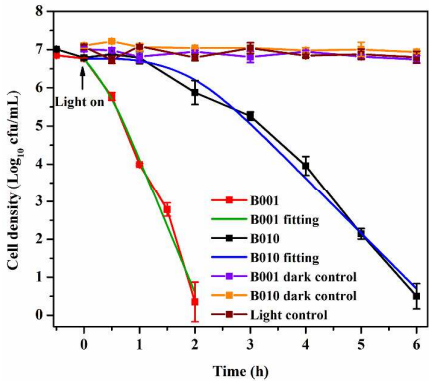

Fig. 4 Photocatalytic inactivation efficiency of *E. coli* K-12 (1×10^7 CFU mL^{-1}) in the presence of B001 and B010 nanosheets under VL irradiation.

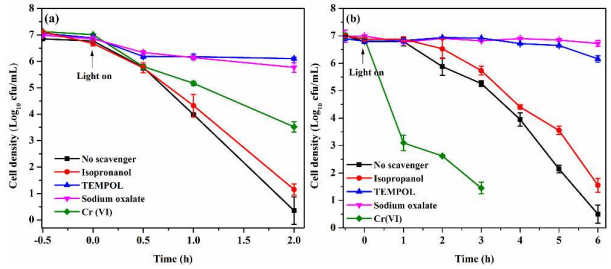

Fig. 5 The photocatalytic inactivation of E. coli K-12 in the presence of different scavengers: no scavenger, 5 mM Isopropanol, 2 mM TEMPOL, 0.5 mM sodium oxalate, and 0.05 mM Cr(VI) for (a) B001 and (b) B010 nanosheets as photocatalysts under VL irradiation.

In order to determine the vibration features and defects of BiOBr nanosheets, the Raman spectra were performed in the range of 50-800 cm^{-1}. Due to the tetragonal PbFCl-type structure with space group P4/nm, the Raman active modes of BiOBr are two A_{1g}, B_{1g} and E_g.[34] The B001 and B010 nanosheets show similar Raman spectra (Fig. 3a). The strongest band located at about 59 cm^{-1} can be attributed to the A_{1g} internal Bi-Br stretching mode, while the band at 113 cm^{-1} also comes from the A_{1g} internal Bi-Br stretching mode.[29,32] The band at 162 cm^{-1} can be assigned to the E_g Bi–Br stretching mode.[32] Moreover, a weak and readily unnoticeable band at 393 cm^{-1} which ascribed to the B_{1g} mode originated from the motion of the oxygen atoms.[34] Notably, the bands appeared at 69 and 91 cm^{-1} can be assigned to the E_g and A_{1g} first-order vibration modes of Bi metal, which is due to the formation of oxygen vacancies in BiOBr nanosheets.[35] More importantly, the intensity of A_{1g} mode at 91 cm^{-1} for the B001 nanosheet is much stronger than the B010 nanosheet, suggesting that B001 nanosheets have more oxygen vacancies on their surface. Fig. 3b shows the powder EPR spectra of B001 and B010 nanosheets at 77° K. No obvious signal is observed for B010 nanosheet. However, a remarkable broad resonance signal is observed at g = 2.16 for B001 nanosheet, which can be attributed to the trapped electrons from oxygen vacancies.[36,37] The result further demonstrates that surfaces in B001 nanosheets contain high density of oxygen vacancies, corresponding to the result of Raman spectra. These oxygen vacancies should be formed during the synthetic process, due to the long bond length and low bond energy of Bi-O band.[38,39] As one kind of point defect, the oxygen vacancy could affect the charge transfer and separation process, thus would play a very important role in the photocatalytic activities of BiOBr nanosheets.

Visible-light-driven (VLD) photocatalytic bacterial inactivation

E. coli K-12, a common waterborne bacterium, was chosen as a representative microorganism to evaluate the facet-dependent photocatalytic inactivation activities of B001 and B010 nanosheets. In the light and dark control experiments, the bacterial population remains unchanged even after 6 h, indicating no toxic effects of B001 and B010 nanosheets to bacterial cells and no photolysis of *E. coli* K-12 cells under VL irradiation (Fig. 4). Surprisingly, the B001 nanosheets are quite effective in inactivating the bacterial cells, with the complete inactivation of cell densities of 10^7 (i.e. 7-log) CFU mL^{-1} within 2 h under VL irradiation. However, when employing the B010 nanosheets as photocatalyst, only 1-log reduction of bacterial cells is obtained within 2 h and only 6.5-log reduction is observed even within 6 h. Obviously, the photocatalytic bacterial inactivation efficiency of B001 nanosheets is remarkably higher than that of B010 nanosheets. Moreover, the kinetics of photocatalytic bacterial inactivation of B001 and B010 nanosheets also differ from each other. The photocatalytic bacterial inactivation kinetics can be well fitted by a "shoulder+log-linear" model[40] with the parameters for the inactivation rate (k_{max}) and the shoulder length (S). In photocatalytic bacterial inactivation process, a shoulder can be reasoned by a cumulative damage through the photocatalytic reactions before the proliferation of a single cell is inhibited.[40] The fitted parameters of the shoulder length S for B001 and B010 nanosheets are 0.23 and 1.86 h, respectively. It is

suggested that the time for B001 nanosheets producing a minimum number of radicals to inhibit the proliferation of bacterial cells is much shorter than that of B010nanosheets. And the inactivation rate constant k_{max}=8.12 h^{-1} of B001 nanosheets is 2.4 times higher than that of B010nanosheets (3.38 h^{-1}), indicating the B001 nanosheets have superior photocatalytic bacterial inactivation activity compared to B010 nanosheets.

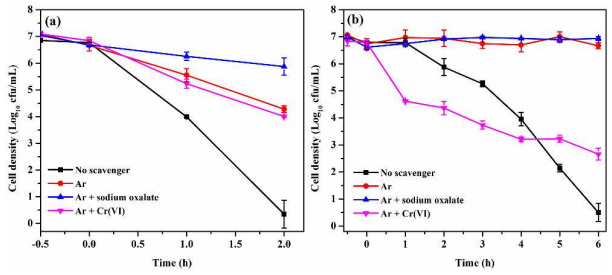

Fig. 6 The photocatalytic inactivation of *E. coli* K-12 in the presence of (a) B001 and (b) B010 nanosheets with argon (Ar) purging under VL irradiation.

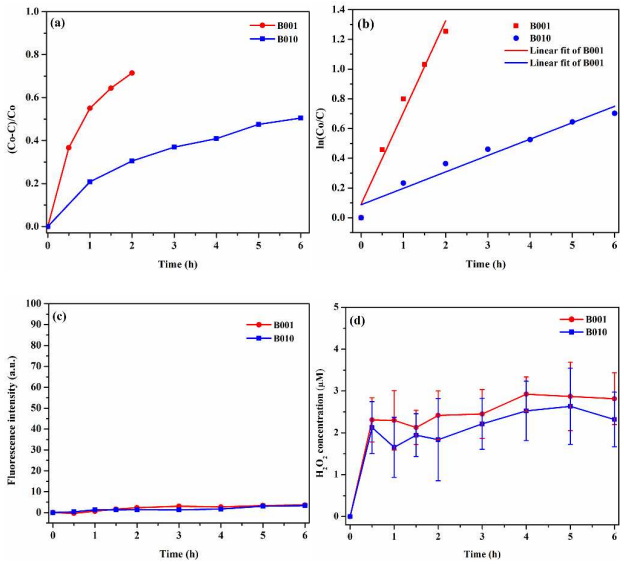

Fig. 7 (a) Transformation percentage and (b) Pseudo-first-order reaction fitting curve of NBT concentration, (c) Fluorescence intensity of TAOH, (d) H_2O_2 concentration in the presence of B001 and B010 nanosheets under VL irradiation.

Facet-dependent VLD bacterial inactivation mechanism

Photocatalytically generated reactive species, such as hole (h^+), electron (e^-), $\bullet O_2^-$ and •OH, were considered to be involved in the photocatalytic bacterial inactivation. To investigate the contributions of different reactive species, the photocatalytic inactivation activities with the addition of different scavenger were compared in detail for B001 and B010 nanosheets. Different scavenging agents were employed individually to remove the specific reactive species.[41,42] Before conducting the scavenging experiments, the concentrations used for each scavenger were optimized to specify their significant effect but would not cause toxicity to the bacterial cells. As shown in Fig. 5a, with the addition of isopropanol as a scavenger for •OH, the bacterial inactivation efficiency has no significant change compared with that of no scavenger added, indicating a minor contribution of •OH in this VLD photocatalytic inactivation process. It is because that the standard redox potential of Bi(V)/Bi(III) (+1.59 eV) is more negative than those of $\bullet OH/OH^-$ (+1.99 eV) and $\bullet OH/H_2O$ (+2.73 eV), the photogenerated h^+ from BiOBr cannot oxidize ambient OH^- to form •OH.[43] However, an obvious inhibitory effect is observed when 4-hydroxy-2,2,6,6-tetramethylpiperidinyloxy (TEMPOL) and sodium oxalate added to remove$\bullet O_2^-$ and h^+, respectively. These phenomena demonstrate that both h^+ and $\bullet O_2^-$ play important roles during the bacterial inactivation process of B001 nanosheets. $\bullet O_2^-$ is usually originated from e^-. Expectedly, the quenching e^- by Cr(VI) results in a significant decrease in the inactivation efficiency, with *ca.* 3.5-log reduction in cell densities. Thus, h^+ and $\bullet O_2^-$are the major reactive species responsible for the VLD photocatalytic inactivation process of B001 nanosheets. Similarly, when employing B010 nanosheet as a photocatalyst, the ignorable inhibition effect of •OH is also determined by the slight decrease of cell densities with *ca.* 1.5-log after adding isopropanol (Fig.5b). The addition of sodium oxalate to eliminate h^+ totally suppresses the inactivation efficiency. Besides, less than 1-log reduction in cell density is observed within 6 h when TEMPOL is added to quench $\bullet O_2^-$. The result implies that both h^+ and $\bullet O_2^-$are also critical in the photocatalytic bacterial inactivation of B010 nanosheets under VL irradiation. It should be pointed out that, after adding Cr(VI) as the scavenger of e^-, the bacterial inactivation efficiency is otherwise significantly enhanced. The toxic effect of Cr(VI) cannot account for such a great variation, as confirmed by the corresponding light and dark controls (Fig. S2). It is assumed that the consumption of e^- by Cr(VI) would remarkably enhance the photogenerated h^+/e^- pair separation efficiency and thus would favor the inactivation process mediated by h^+.

The contributions of $\bullet O_2^-$ and h^+ in inactivation process are further studied under VL irradiation at anaerobic conditions. The solution was purged continuously with argon (Ar) to remove O_2 to avoid the formation of $\bullet O_2^-$, leaving only the function of h^+ and e^-. As illustrated in Fig.6a, purging with Ar can inhibit the bacterial inactivation effect with 4.3-log live cells remaining within 2 h. Then, there is no change of bacterial inactivation after adding Cr(VI), supporting e^- is not the major reactive species involved in the bacterial inactivation. Besides, a decrease of *ca.* 5.9-log in cells density is observed when sodium oxalate is added, demonstrating that the h^+ alone can directly inactivate the bacterial cells. Moreover, *ca.* 5-log reduction of bacterial cells can be obtained when the VLD

photocatalytic inactivation process is prolonged to 6 h (Fig. S3). The calculated parameter k_{max} (1.66 h^{-1}) is smaller than that without Ar aeration (8.12 h^{-1}). It is because photogenerated h^+ stays on the surface of the photocatalysts and cannot move into the reaction solution, resulting in a rather limited contact with the bacterial cells. It is worth mentioning that the calculated parameter S applying the "shoulder+log–linear" model is negative, suggesting a rapid inactivation that can instantly kill bacteria cells without any inhibition period. This can be ascribed to an increasing amount of photogenerated h^+ since it is a more powerful oxidant than other reactive species.[44] On the contrary, h^+ almost makes no contribution to the bacterial inactivation in B010 system under the anaerobic condition (Fig. 6b). The cell density also keeps unchanged within 6 h after adding sodium oxalate. Similarly, bacterial inactivation is significantly enhanced by addition of Cr(VI), compared with that without Ar aeration (Fig. 4b). These results further support the importance of h^+ after removed e^- by addition of Cr(VI).As a consequence, the photogenerated$\bullet O_2^-$ and h^+ are suggested as the dominant reactive species both in B001 and B010 systems in the VLD bacterial inactivation process.

The contributions of $\bullet O_2^-$ and •OH in the bacterial inactivation are further quantitatively clarified using NBT and TA as the $\bullet O_2^-$ and •OH probe, respectively.[22] As shown in Fig. 7a, the concentration of $\bullet O_2^-$in B001 nanosheet system quickly increases within 2 h under VL irradiation. Nevertheless, the increase of $\bullet O_2^-$ in B010 system is quite slow and the concentration of $\bullet O_2^-$is still low even prolonging irradiation time to 6 h. In addition, the photoreaction process of NBT is found to be well fit a pseudo-first-order kinetics (Fig. 7b), with the rate constant k of 0.616 h^{-1} (R^2= 0.965) and 0.11 h^{-1} (R^2= 0.946) for B001 and B010 nanosheets, respectively. According to the reaction equation,[45] the yield of $\bullet O_2^-$is 2.46 h^{-1} for B001 nanosheets, which is 5.6 times of that for B010 nanosheets (0.44 h^{-1}). However, no measurable •OH can be detected in the bacterial inactivation process both in the presence of B001 and B010 nanosheets (Fig. 7c), which is consistence with the results of scavenger studies. The H_2O_2 production is also directly monitored using the microplate fluorometric method.[33] As shown in Fig.7d, the concentrations of H_2O_2 quickly increase and become constant with prolonged irradiation time in both BiOBr nanosheet systems. In addition to the inability of •OH production from h^+ aforementioned, $\bullet O_2^-$is proved to be important in the bacterial inactivation and H_2O_2 should be primarily generated from $\bullet O_2^-$. Meanwhile, a slightly higher concentration of $H_2O_2$is observed in B001 system, which is due to the higher concentration of initial $\bullet O_2^-$.

To further compare the production and confirm the existence of $\bullet O_2^-$, the ESR measurements were carried out using 5,5-dimethyl-1-pyrroline N-oxide (DMPO) as a spin-trap for $\bullet O_2^-$.[23] As shown in Fig. 8a, no resonance signals are detected for samples in dark. Under VL irradiation, both B001 and B010 nanosheets exhibit a characteristic signal for the DMPO-$\bullet O_2^-$ spin adduct, validating the generation of $\bullet O_2^-$ for the two samples. Moreover, a stronger signal is observed for B001 nanosheets, implying that more $\bullet O_2^-$ are produced over B001 than B010 nanosheets, in agreement with the result of Fig. 7a. As discussed above, oxygen vacancies are formed over the B001 nanosheets, which should strongly affect their band structures leading to different behavior of resulting reactive species. UV-vis spectra show that B001 and B010 nanosheets possess approximate adsorption characteristics in the whole wavelength range (Fig. S4a). Nevertheless, the band gap energy (E_g) (Fig. S4b) of B001 nanosheet is 2.80 eV, slightly smaller than that of B010 nanosheet (2.85 eV), owing to the higher amount of oxygen vacancies existed in B001 nanosheet.[39] The valence band XPS was carried out to determine the band edges, as illustrated in Fig. 8b. The B010 nanosheet displays a VB maximum energy (E_{VB}) at about 2.45 eV, while the CB minimum energy (E_{CB}) occurs at about -0.4 eV, according to the equation $E_g = E_{VB} - E_{CB}$. On the contrary, the E_{VB} of B001 nanosheet is up-shifted to 2.31 eV and the E_{CB} was calculated to be -0.51 eV by up-shifts accordingly. As the VB width intrinsically controls the mobility of h^+, the increased VB width is in favor of the separation of photogenerated charges.[31] Thus, the wider VB width of B001 nanosheet leads to higher mobility and better photo-oxidation of h^+. On the other hand, the raised E_{CB} results in the inhibiting of the h^+/e^- pair recombination, owing to the faster transfer of photoexcited e^- to reactants.[39]

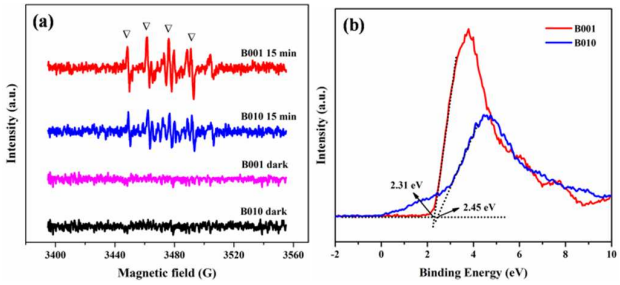

Fig. 8 (a) EPR spectra of DMPO-$\bullet O_2^-$ generated by B001 and B010 nanosheets before and under VL irradiation; (b) Valence-band XPS spectra of B001 and B010 nanosheets.

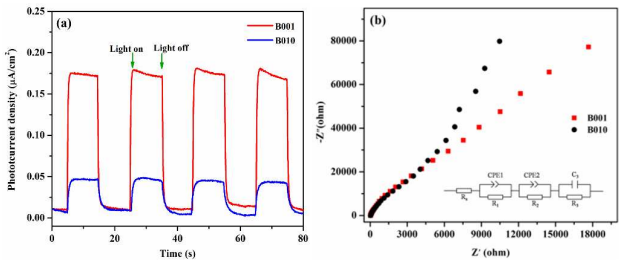

Fig. 9 (a) Transient photocurrent responses and (b) electrochemical impedance spectra (the equivalent circuit is shown as an inset in the figure) of B001 and B010 nanosheets under VL irradiation.

It is also of significance to further understand the separation and transfer of photogenerated e^-/h^+ pairs for the two kinds of BiOBr nanosheets. The transient photocurrent responses of B001and B010 nanosheets are recorded with several on/off cycles of intermittent VL irradiation. As can be seen in Fig. 9a, B001

nanosheets present a distinctly higher current density, about 4 times than that of B010 nanosheets. The increased current density manifests an enhancing the separation efficiency of the photoinduced e^-/h^+ pairs, which would result in a higher photocatalytic performance.[46] The EIS measurements are also employed to investigate the electron transfer resistance and the separation efficiency between the photogenerated e^-/h^+ pairs. The smaller arc radius of the Nyquist plot are, the higher efficiency of interfacial charge transfer and the more effective separation of photogenerated e^-/h^+ pairs will be.[24] Compared with B010 nanosheets, B001 nanosheets clearly display a smaller arc radius (Fig. 9b), which means a more effective interfacial charge transfer and separation of photogenerated e^-/h^+ pairs. Moreover, resistances of the work electrode (R1) for the equivalent circuit (insert in Fig. 9b) are 9157 and 12590 Ω for B001 and B010, respectively (Table S1).The result demonstrates that the work electrode of B001 has higher conductivity, which can facilitate kinetic charge transfer.[47]

Thus, the highly facet-dependent bacterial inactivation were attempted in the different amount of $\bullet O_2^-$ and h^+ between B001 and B010nanosheets.B001 nanosheets can photogenerate higher amount of h^+ and e^- than B010 nanosheets in the same period of time. More $\bullet O_2^-$ can be subsequently derived from e^- for B001 nanosheets. Simultaneously, more O_2 in the environment can be activated by oxygen vacancies for B001 nanosheets to produce more $\bullet O_2^-$. In fact, the amount of $\bullet O_2^-$ and/or h^+ is high enough to suppress the influence of surface area (Fig. S5), which potentially affects the contact between photocatalysts and bacterial cells. Consequently, in B001 system, either the amount of $\bullet O_2^-$ and/or h^+ is high enough to individually damage bacterial cells within 2 h under VL irradiation, i.e. a large amount of $\bullet O_2^-$ and/or h^+ can quickly accumulate in a short time so that B001 nanosheets can photocatalytically inactivate 7-log bacterial cells only within 2 h. Comparatively, in B010 system, neither the amount of $\bullet O_2^-$ nor that of h^+ is high enough to photocatalytically inactivate all bacterial cells in 6 h. It is reasonable to state that the accumulating time of high enough amount of $\bullet O_2^-$ and/or h^+ is very long in B010 nanosheets system, so that only 6.5-log bacterial cells can be inactivated even within 6 h VL irradiation.

Based on the above results, the VLD photocatalytic mechanism for the obviously different bacterial inactivation activities is proposed for B001 and B010 nanosheets (Fig. 10). Theoretical calculations suggest that {001} facet has a lower recombination rate of e^-/h^+ pairs than that of {010} facet for BiOBr.[48] Meanwhile, BiOBr has a unique layer structure with $[Bi_2O_2]$ slabs interleaved with double slabs of Br atoms. This would lead to a non-uniform charge distribution between $[Bi_2O_2]$ and Br slices, resulting in the generation of an internal electric field (IEF) along the [001] direction.[49,50] The IEF is perpendicular to the {001} facet of B001 nanosheets, but parallel to the {010} facet of B010 nanosheets. Hence, BiOBr nanosheets with {001} facet have a shorter charge diffusion distance assisted by IEF. Simultaneously, oxygen vacancies act as a deep defect level between CB and VB, promoting the separation efficiency of photogenerated h^+/e^- pairs.[39] Thereby, the separation and transfer of photogenerated e^-/h^+ pairs are more favorable for B001 nanosheets than that for B010 nanosheets. Consequently, a large amount of h^+ for B001 nanosheets is accumulated in a short time so that it can inactivate bacteria individually, while a small amount of h^+ for B010 nanosheets cannot efficiently inactivate bacteria. On the other hand, faster charge separation process of B001 system makes photogenerated e^- to react with molecular O_2 to produce a larger amount of $\bullet O_2^-$. Furthermore, oxygen vacancies with trapped electrons are active sites for easy adsorption of the O_2 molecule.[39] B001 nanosheets with more oxygen vacancies can activate more molecular $O_2$to produce $\bullet O_2^-$. The oxygen vacancies induced O_2activation processes for B001 and B010 nanosheets are also different. Oxygen molecules in environment can be absorbed on {001} facet via one-electron transfer pathway, whereas the adsorption of oxygen on the {010} facet are through two-electron transfer pathway,[34] thus resulting in a higher production rate of $\bullet O_2^-$. Consequently, the amount of $\bullet O_2^-$ generated by B001 nanosheets is much greater than that generated by B010 nanosheets. Inevitably, the accumulation period of h^+ and $\bullet O_2^-$ is shorter in B001 system than that in B010 system. That is why B001 nanosheets can completely inactivate 7-log bacterial cells within 2 h due to a large amount of h^+ and $\bullet O_2^-$ produced, whereas B010nanosheets can only inactivate 6.5-log bacterial cells even within 6 h accounted for limited production of h^+ and $\bullet O_2^-$.

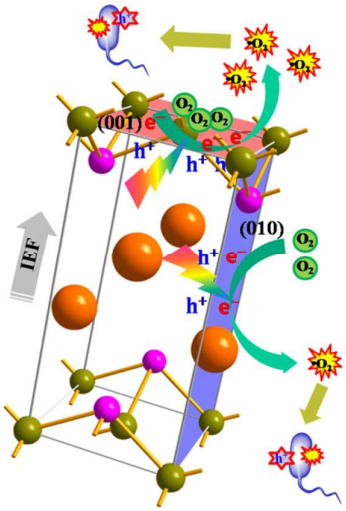

Fig. 10 Proposed mechanism of facet-dependent VLD bacterial inactivation of BiOBr nanosheets.

Conclusions

In summary, BiOBr nanosheets with dominantly exposed {001} and {010} facets are synthesized via a simple hydrothermal method, respectively. Significant differences in the VLD photocatalytic inactivation of *E. coli* K-12 for B001 and B010 nanosheets are compared systematically. The h^+ and $\bullet O_2^-$ are believed as the major reactive species responsible for the bacterial inactivation both in the B001 and B010 photocatalytic

systems. However, the B001 nanosheets exhibit a remarkably higher photocatalytic bacterial inactivation than that of B010 nanosheets. That is, B001 nanosheets can completely inactivate 7-log bacterial cells within 2 h, whereas B010nanosheets can only inactivate 6.5-log bacterial cells even within 6 h. The enhancement of bacterial inactivation efficiency is mainly attributed to the accumulation of the reactive species ($\bullet O_2^-$ and h^+)within a short time, due to the more oxygen vacancies and the faster separation and transfer of photogenerated e^-/h^+ pairs.

Acknowledgements

This work was supported by grants from the General Research Fund (GRF 476811) of the Research Grants Council and the ITSP Tier 3 Scheme (ITS/273/13) of Innovation Technology Commission, Hong Kong SAR Government, Hong Kong, National Natural Science Funds for Distinguished Young Scholars (41425015) and National Science Foundation of China (21077104). P.K. Wong wants to express his thanks to the CAS/SAFEA International Partnership Program for Creative Research Teams of Chinese Academy of Sciences, China. The authors would also like to acknowledge the technical support provided by Analytical and Testing Center, Huazhong University of Science and Technology, China.

Notes and references

1 A. Kubacka, M. Fernandez-Garcia and G. Colon, *Chem. Rev.*, 2011, **112**, 1555-1614.
2 A. Kudo and Y. Miseki, *Chem. Soc. Rev.*, 2009, **38**, 253-278.
3 F. Zuo, K. Bozhilov, R.J. Dillon, L. Wang, P. Smith, X. Zhao and P. Feng, *Angew. Chem.*, 2012, **124**, 6327-6330.
4 Z.Y. Jiang, Q. Kuang, Z.X. Xie and L.S. Zheng, *Adv. Funct. Mater.*, 2010, **20**, 3634-3645.
5 G. Liu, C.Y. Jimmy, G.Q.M. Lu and H.M. Cheng, *Chem. Comm.*, 2011, **47**, 6763-6783.
6 Y. Bi, S. Ouyang, N. Umezawa, J.Cao and J. Ye, *J. Am. Chem. Soc.*, 2011, **133**, 6490-6492.
7 J. Yu, J. Low, W. Xiao, P. Zhou and M. Jaroniec, *J. Am. Chem. Soc.*, 2014, **136**, 8839-8842.
8 R. Li, F. Zhang, D. Wang, J. Yang, M. Li, J. Zhu and C. Li, *Nature Comm.*, 2013, **4**, 1432.
9 R. Boppella, K. Anjaneyulu, P. Basak and S.V. Manorama, *J. Phys. Chem. C*, 2013, **117**, 4597-4605.
10 B. Wang, S. Shen and L. Guo, *Appl. Catal. B: Environ.*, 2015, **166–167**, 320–326.
11 Y.P. Xie, G. Liu, L. Yin and H.M. Cheng, *J. Mater. Chem.*, 2012, **22**, 6746-6751.
12 Q. Liang, H. Zhao, L. Ning, J. Wang, C. Zhang, A. Wei and H. Yang, *Appl. Catal. B: Environ.*, 2014, **152**, 390-396.
13 G. Wang, X. Ma, B. Huang, H. Cheng, Z. Wang, J. Zhan and Y. Dai, *J. Mater. Chem.*, 2012, **22**, 21189-21194.
14 J. Jiang, K. Zhao, X. Xiao and L. Zhang, *J. Am. Chem. Soc.*, 2012, **134**, 4473-4476.
15 L. Zhang, J. Shi, M. Liu, D. Jing and L. Guo, *Chem. Comm.*, 2014, **50**, 192-194.
16 H. Zhao, W. Yin, M. Zhao, Y. Song and H. Yang, *Appl. Catal. B: Environ.*, 2013, **130**, 178-186.
17 H. Wang, J. Yang, X. Li, H. Zhang, J. Li and L. Guo, *Small*, 2012, **8**, 2802-2806.
18 J. Chen, G. Li, H. Zhang, P. Liu, H. Zhao and T. An, *Catal. Today*, 2014, **224**, 216-224.
19 H. G. Yang, C. H. Sun, S. Z. Qiao, J. Zou, G. Liu, S. C. Smith, H. M. Cheng and G. Q. Lu, *Nature*, 2008, **453**, 638-641.
20 H. Tong, S. Ouyang, Y. Bi, N. Umezawa, M. Oshikiri and J. Ye, *Adv. Mater.*, 2012, **24**, 229-251.
21 H. Cheng, B. Huang and Y. Dai, *Nanoscale* 2014, **6**, 2009-2026.
22 L. Ye, Y. Su, X. Jin, H. Xie and C. Zhang, *Environ. Sci.: Nano*, 1 (2014) 90-112.
23 H. Huang, X. Li, X. Han, N. Tian, Y. Zhang and T. Zhang, *Phys. Chem. Chem. Phys.*, 2015, **17**, 3673-3679.
24 H. Huang, X. Han, X. Li, S. Wang, P.K. Chu, and Y. Zhang, *ACS Appl. Mater. Interfaces*, 2015, **7**, 482-492.
25 L. Jing, W. Zhou, G. Tian and H. Fu, *Chem. Soc. Rev.*, 2013, **42**, 9509-9549.
26 H. Zhang, Y. Yang, Z. Zhou, Y. Zhao and L. Liu, *J. Phys. Chem. C*, 2014, **118**, 14662-14669.
27 W. Lin, X. Wang, Y. Wang, J. Zhang, Z. Lin, B. Zhang and F. Huang, *Chem. Comm.*, 2014, DOI: 10.1039/C3CC41498A
28 Z. Liu, B. Wu, J. Niu, X. Huang and Y. Zhu, *Appl. Surf. Sci.*, 2014, **288**, 369-372.
29 D. Zhang, J. Li, Q. Wang and Q. Wu, *J. Mater. Chem. A*, 2013 **1**, 8622-8629.
30 H. Li, J. Liu, X. Liang, W. Hou and X. Tao, *J. Mater. Chem. A*, 2014, **2**, 8926-8932.
31 J. Chen, M. Guan, W. Cai, J. Guo, C. Xiao and G. Zhang, *Phys. Chem. Chem. Phys.*, 2014, **16**, 20909-20914.
32 J. Wang, Y. Zhang, L. Tian, F. Liu and Q. Xia, *J. Nanopart. Res.*, 2014, **16**, 1-10.
33 M.E. Abbas, W. Luo, L. Zhu, J. Zou and H. Tang, *Food Chem.*, 2010, **1**, 327-331.
34 K. Zhang, J. Liang, S. Wang, J. Liu, K. Ren, X. Zheng and X. Yu, *Cryst. Growth Design*, 2012, **12**, 793-803.
35 J. Hu, W. Fan, W. Ye, C. Huang and X. Qiu, *Appl. Catal. B: Environ.*, 2014, **158**, 182-189.
36 X. Zhou, J. Qu,F. Xu, J. Hu, J.S. Foord, Z. Zeng, X. Hong and S.C.E. Tsang, *Chem. Commun.*, 2013, **49**, 1747-1749.
37 P. Chetri, B. Choudhury and A. Choudhury, *J. Mater. Chem. C*, 2014, **2**, 9294-9302.
38 L. Ye, L. Zan, L. Tian, T. Peng and J. Zhang, *Chem. Commun.*, 2011, **47**, 6951-6953.
39 M. Guan, C. Xiao, J. Zhang, S. Fan, Ran An, Q, Cheng, J. Xie, M. Zhou, B. Ye and Y. Xie, *J. Am. Chem. Soc.*, 2013, **135**, 10411-10417.
40 H. Schwegmann, J. Ruppert and F.H. Frimmel, *Water Res.*, 2013, **47**, 1503-1511.
41 L.S. Zhang,; K.H. Wong,; H.Y. Yip, C. Hu, J.C. Yu, C.Y. Chan and P.K. Wong, *Environ. Sci. Technol.*, 2010, **44**, 1392-1398.
42 W. Wang, T.W. Ng, W.K. Ho, J. Huang, S. Liang, T. An and P.K. Wong, *Appl. Catal. B: Environ.*, 2013, **129**, 482-490.
43 J. Fu, Y. Tian, B. Chang, F. Xi and X. Dong, *J. Mater. Chem.*, 2012, **22**, 21159-21166.
44 G. Li, X. Liu, H. Zhang, P.K. Wong, T. An and H. Zhao, *Appl. Catal. B: Environ.*, 2013, **140**, 225-232.
45 L. Ye, C. Gong, J. Liu, L. Tian, T. Peng, K. Deng and L. Zan, *J. Mater. Chem.*, 2012, **22**, 8354-8360.
46 H. Lin, X. Li, J. Cao, S. Chen and Y. Chen, *Catal. Comm.*, 2014, **49**, 87-91.
47 Y. Zhou, X. Zhang, Q. Zhang, F. Dong, F. Wang and Z. Xiong, *J. Mater. Chem. A*, 2014, **2**, 16623-16631.
48 H. Zhang, L. Liu and Z. Zhou, *RSC Adv.*, 2012, **2**, 9224-9229.
49 J. Li, Y. Yu and L. Zhang, *Nanoscale*, 2014, **6**, 8473-8488.
50 K. Zhao, L. Zhang, J. Wang, Q. Li, W. He and J.J. Yin, *J. Am. Chem. Soc.*, 2013, **135**, 15750-15753.

TOC:

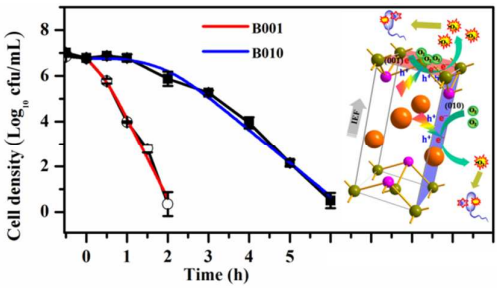

Text:

The efficiency of photocatalytic inactivation towards *Escherichia coli* K-12 is highly dependent on the dominantly exposed facets of BiOBr.